Ab initio calculations of grain boundaries in W, Mo, Fe and W25at%Re

Daniel Scheiber*[1,2], Reinhard Pippan[3], Peter Puschnig[2] and Lorenz Romaner[1]

[1] Material Center Leoben Forschung GmbH, Roseggerstrasse 12, 8700 Leoben, Austria
[2] University of Graz, Institute of Physics, NAWI Graz, Universitätsplatz 5, 8010 Graz, Austria
[3] Erich Schmid Institut of Materials Science, Austrian Academy of Sciences, Jahnstrasse 12, 8700 Leoben, Austria

* Email: daniel.scheiber@mcl.at; Phone: +43 3842 45922-511

Abstract. In this study we compute grain boundary (GB) properties for a large set of GBs in bcc transition metals with a special focus on W, Mo, Fe and W25at%Re using ab initio density functional theory (DFT) and semi-empirical second nearest neighbour modified embedded atom method (2NN-MEAM) potentials. The GB properties include GB energies, surface energies, work of separation and GB excess volume. We first identify the best simulation setup to evaluate these properties and then analyse them and compare them to various experimental data where we find a good overall agreement. In particular our results explain the experimental finding that W and Mo prefer intergranular fracture while other bcc metals prefer transgranular cleavage. We find that the used 2NN-MEAM potentials can predict general trends of GB properties but do not always reproduce the GB ground state structure and energy found with DFT.

1   Introduction

Refractory metals are important for many applications, for example high temperature applications including use in future fusion reactors, corrosion resistant materials, or applications demanding a high hardness. Most bcc refractory metals exhibit a change from ductile-to-brittle fracture with decreasing temperature and in the brittle regime fracture is dominated, especially for polycrystalline W and Mo, by the strength of grain boundaries (GBs).

Grain boundaries have long posed a serious challenge for ab initio methods because large numbers of atoms are needed to accurately model such extended defects. For this reason, many studies on GBs use computationally less demanding semi-empirical potentials. Especially for bcc metals, second nearest neighbour modified embedded atom method (2NN-MEAM) potentials have been widely used, for e.g. the calculation of GB structures [1], [2], GB and surface energies [3]–[5], segregation and

embrittlement at GBs [6], [7]. Despite their computational convenience, semi-empirical potentials have a drawback: They are parametrized to certain material properties (typically elastic constants, vacancy energies, etc.) and it is unclear whether the parametrization is equally valid for other properties, in particular GB structures and energies.

Contrary to semi-empirical potentials, ab-initio density functional theory (DFT) does not depend on parametrization to a specific material, but achieves highly precise results due to an explicit quantum-mechanical treatment of the underlying electronic structure problem. Despite these advantages, DFT investigations commonly deal only with one or two GBs at a time [8]–[12]. It is a debatable point whether the results can be extrapolated to real polycrystalline materials containing a huge variety of GBs. Furthermore, systematic investigations of trends within a whole material class are rare.

In this work, we provide a comprehensive overview of GB energies and GB structures in the bcc transition metals. A large number of GBs are considered in the materials W, Mo and Fe with DFT and 2NN-MEAM. In this way, we establish how closely 2NN-MEAM calculations agree with DFT results and investigate if it is possible to save computational effort by suitably combining the two methods. In this context we wrap up a long-standing discussion [8], [13]–[15] about the translation state of the Σ5[1-10](013) GB, for which we also considered the metals Ta, Nb, V. We also include an alloy in our material selection, W25at%Re, which we model on the basis of the virtual crystal approximation (VCA) [16], [17]. We do not include here the effect of Re enrichment at GBs due to segregation; The interested reader is here referred to Ref. [18].

The large number of treated materials and GBs allows for an unprecedented comparison to experimental data available in literature. We focus on important properties including GB energy, surface energy, work of separation and GB excess volume. Finally, we condense the GB results to assess the tendency for inter- or transgranular fracture for bcc transition metals and compare to experimental evidence. For a more complete picture, we include here also MEAM results for the metals Ta, Nb, Cr and V.

2   Methodology

2.1   Computational details

Two simulation methods are used in this study: ab-initio DFT and semi-empirical 2NN-MEAM potential simulations. DFT computations were performed with VASP [19]–[26] using projector augmented wave functions (PAW) and the exchange-correlation (xc) functional PBEsol [27]. The VCA is implemented in the PAW approach as described in previous studies [28], [29] by creating PAWs for virtual atoms. These virtual atoms possess an intermediate electron and nucleus number that interpolate between the two elements. We found that for an accurate treatment of the transition metals, p semi core electrons must be included as valence electrons leading to 11 valence electrons for Ta, Nb and V, 12 valence electrons for W and Mo and 14 valence electrons for Fe, which we treat in a ferromagnetic manner. In the VCA treatment of W25at%Re, 12.25 electrons were used in the valence. The convergence criterion for ionic relaxation was 0.01 eV/ Å.

For 2NN-MEAM potential simulations, we used parameters published in Ref. [30] and the LAMMPS environment [31], [32]. 2NN-MEAM potentials include contributions from the second nearest neighbours in contrast to conventional MEAM potentials. These contributions are necessary for bcc elements, as in this crystal structure the first nearest neighbour distance is only slightly smaller than the second nearest neighbour distance and the interaction with the second nearest neighbours is not

negligible. For convenience, we will refer to the 2NN-MEAM potentials simply as MEAM in the following.

All structures used for this study were built with the python ASE package [33].

2.2   Convergence study

To compute the GB energy, we investigated three different simulation setups: the fixed grain distance setup (FGD), the cell relaxation setup (CR) and the vacuum on top setup (VOT). The schematic representations of the unit cells for these setups are shown in Figure 1 (FGD, CR) and Figure 2 (VOT). The first setup is FGD, which, because of the periodic boundary conditions, contains two GBs. The atoms are relaxed without restriction and the cell size is kept fixed. Therefore, we are neglecting that in the starting configurations the grains may not be in equilibrium distance, which might introduce stress in the cell. The CR is identical to FGD with the only difference that the cell is also relaxed to completely remove stress in the unit cell. By that the grain distance can change to its equilibrium value. Due to the arising Pulay stress a higher energy cut-off is needed in CR calculations. Finally, in the VOT setup a vacuum slab is introduced on top of the GB cell. The relaxation of the grain boundary distance is here absorbed by the vacuum. An advantage of the VOT setup is that it can deal with asymmetric GBs where two different surfaces meet at the GB, which is not possible with the two other setups (FGD and CR).

The GB energy γ_{GB} is calculated as

$$\gamma_{GB}^{FGD} = \frac{E_{GB}^{FGD} - E_{Bulk}^{FGD}}{2\,A}, \qquad \gamma_{GB}^{CR} = \frac{E_{GB}^{CR} - E_{Bulk}^{CR}}{2\,A}, \qquad \gamma_{GB}^{VOT} = \frac{E_{GB}^{VOT} - E_{FS}^{VOT}}{A}, \qquad 2.1$$

where A denotes the area of the GB and E the total energy of the unit cell. The free surface energy γ_{FS} is computed using

$$\gamma_{FS} = \frac{E_{FS}^{setup} - \frac{N_{FS}}{N_{Bulk}} E_{Bulk}^{setup}}{2\,A}, \qquad 2.2$$

where N_{FS} and N_{Bulk} are the number of atoms in the corresponding free surface structure and the bulk structure, respectively, and the *setup* tag is replaced by the corresponding setup. Note that in Eq. 2.1 all cells contain the same number of atoms while in Eq. 2.2 this is not the case and scaling with N_{FS}/N_{Bulk} is necessary. The ideal work of separation W_{sep} is the reversible energy needed to separate two grains, which is an important parameter in fracture mechanics [35] and can be simply obtained from the two quantities defined above:

$$W_{sep} = 2\gamma_{FS} - \gamma_{GB}. \qquad 2.3$$

The precise calculation of these quantities within DFT requires a convergence analysis with respect to a set of computational parameters, which we have carried out for the Σ3[1-10](111) tilt GB in W (see Appendix A). The results are summarized in Table 1. This set of converged parameters provides the basis for all other GB calculations in this work. The k-point mesh is transferred to other GBs by scaling it according to the different cell dimensions, and the energy cut-off is always the default for the chosen potential.

To highlight the sensitivity of the results on the choice of xc-functional, we also provide a corresponding analysis in Appendix B for W. The results from the Perdew-Burke-Enzernhof functional improved for solids (PBEsol) and the local density approximation (LDA) match very well the experimental results for lattice parameter and elastic properties, while the Perdew-Burke-Enzernhof functional (PBE) overestimates lattice parameter and underestimates elastic moduli. The

differences for GB properties are particularly pronounced for the work of separation which is about 0.6 J/m2 higher for PBEsol and LDA with respect to PBE. This strong differences underline the importance of using PBEsol rather than PBE.

Further, we compare lattice constants for all elements in this study as obtained by DFT (PBEsol) and MEAM to the experimental data in Appendix C. Since MEAM potentials are fitted to the experimental lattice parameter they correspond closely to experiment. The deviations observed for PBEsol are typical for this functional [34].

The convergence of γ_{GB}, γ_{FS} and W_{sep} with respect to the grain thickness using the three different setups is shown in Figure 3. All three methods converge γ_{GB} to the same value of 2.42 J/m², but with different speed. The CR setup gives sufficiently converged values at 40 Å grain thickness and the VOT setup already at 30 Å, while the FGD setup still overestimates γ_{GB} by 0.03 J/m² at 75 Å. The slower convergence of the FGD setup is a result of the fixed cell size which allows no relaxation in z-direction at the GB. Hence, the relaxation is done at cost of compressing the bulk which causes the slow convergence.

For the evaluation of γ_{FS}, there exists no essential difference between the three methods. The VOT has twice the thickness of the FGD and the CR setup since two grains are contained in the unit cell. In any case, the convergence of γ_{FS} is much faster: already at 10 Å grain thickness the converged value of 3.89 J/m² is obtained. Hence, convergence of γ_{FS} does not represent a critical issue.

The convergence for W_{sep} is linked to the convergence of both γ_{GB} and γ_{FS}. Therefore, the VOT setup shows again the fastest convergence to the value 5.34 J/m² and is, thus, identified as the most convenient method in terms of convergence with cell size.

To further compare the performance of the different setups, we summarize the computation time for the GB energy calculations in Table 2. The computation time is largest for the FGD setup because of the large grain thickness needed for a converged result, followed by the CR setup due to the required high energy cut-off. The least computational effort for a converged result is needed for the VOT setup. Since it allows also treating asymmetric GBs it is, herewith, identified as the most convenient and flexible setup and is employed in this work for all subsequent GB calculations.

Table 1: Converged Parameters for the Σ3[1-10](111) tilt GB in W.

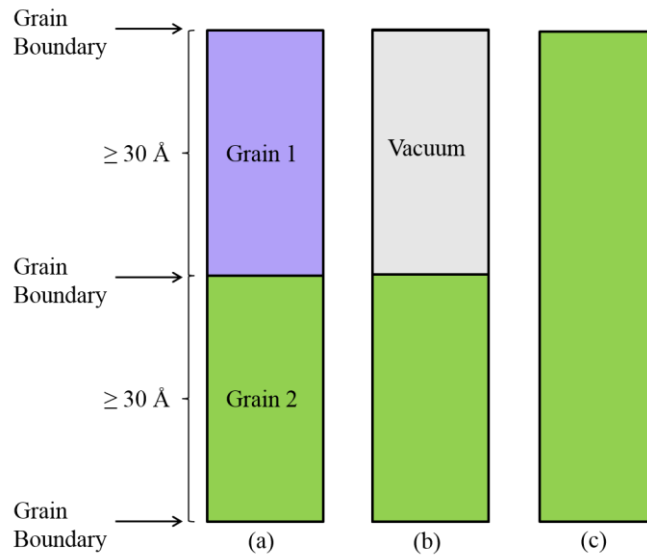| Parameter	Value
k-Point mesh	7x7x1
Energy Cut-off	223 eV
Vacuum thickness	6 Angstrom minimum

Figure 1: Simulation setup for the FGD setup. Figure (a) is a schematic depiction of the GB simulation cell with two GBs. Figure (b) contains two free surfaces and Figure (c) is the reference bulk configuration.
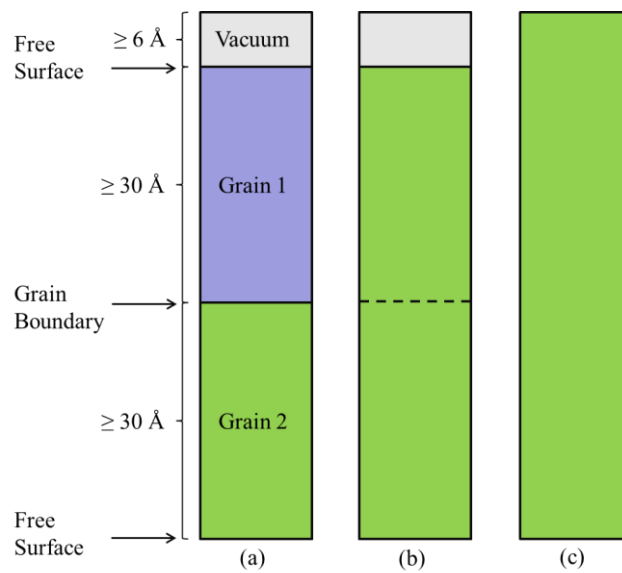

Figure 2: Simulation setup for the VOT setup. Figure (a) is a schematic depiction of the GB simulation cell with a GB, two free surfaces and vacuum on top with the minimum sizes of grains and vacuum. Figure (b) contains two free surfaces and Figure (c) is the reference bulk configuration.
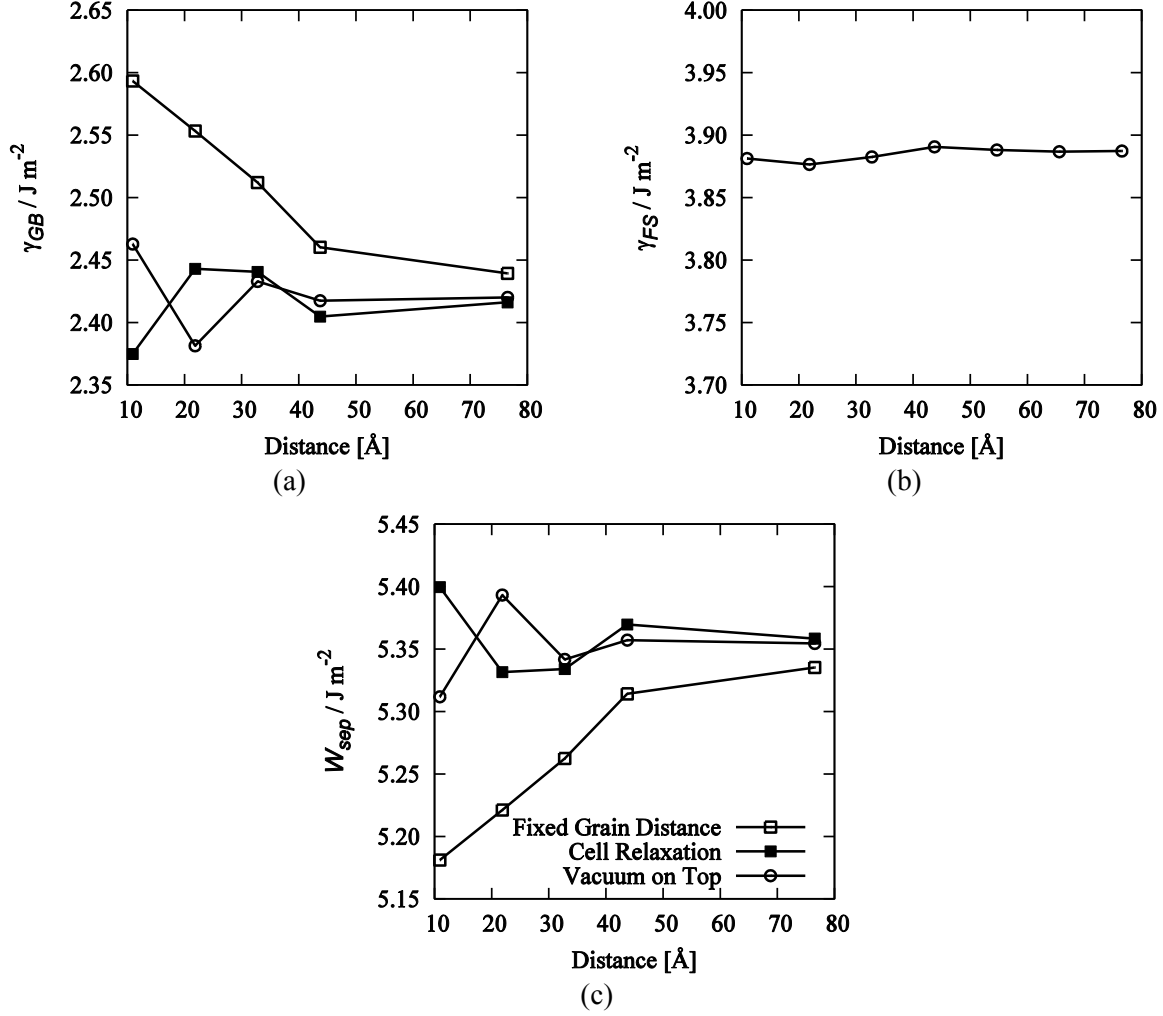
Figure 3: Convergence of (a) γ_{GB}, (b) γ_{FS} and (c) W_{sep} with respect to the distance between interfaces for the $\Sigma 3[1\text{-}10](111)$ tilt GB in W.

Table 2: Comparison of CPU-Time needed for convergence for the different simulation setups.

Setup	CPU-Time / core-hours	Cut-off energy / eV	Grain thickness / Å
Fixed Grain Distance	704	223	75
Cell Relaxation	510	400	40
Vacuum on Top	177	223	30

2.3   γ–surface approach

To obtain the equilibrium ground state structure of a GB, a γ-surface approach is employed for every GB. Herein, the two grains of a GB are shifted with respect to each other on a grid with a maximum spacing of one fourth of the lattice constant. At each shift, we performed ionic relaxations of the atoms without restriction. In this way, we obtained a GB energy for each shift yielding a set of metastable states for each GB, wherein the structure of lowest energy corresponds to the ground state. For the smaller GBs ($\Sigma 3, \Sigma 5, \Sigma 7, \Sigma 9, \Sigma 11$ GBs) the whole grid was computed with MEAMs and DFT, where for DFT we changed the grain thickness to 10 Å to speed up calculations and recalculated the lowest energy structure with 30 Å grain thickness. For computational reasons, the larger GBs ($\Sigma 17, \Sigma 19, \Sigma 33, \Sigma 43$ GBs) were first calculated with MEAM and then the relevant features in the γ–surface were calculated with DFT.

6

3   Results and discussion

This section is grouped in four subsections: first, we investigate and compare the GB energies and the corresponding structures for different GBs and different elements from DFT and MEAM; second and third, we compute for the same GBs the free surface energy and the work of separation again with DFT and MEAM; and fourth, we use our computed GB properties to evaluate the tendency for inter- or transgranular fracture of the elements investigated. Wherever possible, our computed results are compared to available experimental data. A complete list of GBs studied with DFT in this work is given in Table 3. It contains a set of [1-10] tilt GBs, for which the misorientation angle increases gradually from 20° to 150°. For W, a Σ27 GB is also included in this set for comparison with previous works [12], [36]. A smaller set was considered for Fe due to the higher computational effort associated with the spin-polarized calculations. Furthermore, for all metals also other GBs of twist and tilt character are considered since they are frequently discussed in literature. For MEAM the full list of GBs was treated for all metals where the set of [1-10] tilt GBs was treated with a finer resolution (with respect to misorientation angle).

Table 3: List of GBs for each element that has been computed with DFT in this study along with the misorientation angle θ for the [1-10] tilt GBs and the number of atoms in the GB cell.

Grain boundary	θ /°	# of atoms	W	W25at%Re	Mo	Fe
[1-10] tilt GBs						
Σ33[1-10](118)	20.1	132	X	X	X	
Σ19[1-10](116)	26.5	152	X	X	X	X
Σ9[1-10](114)	38.9	72	X	X	X	X
Σ11[1-10](113)	50.5	132	X	X	X	X
Σ3[1-10](112)	70.5	48	X	X	X	X
Σ43[1-10](335)	80.6	258	X	X	X	
Σ17[1-10](223)	86.6	136	X	X	X	X
Σ17[1-10](334)	93.4	136	X	X	X	
Σ3[1-10](111)	109.5	72	X	X	X	X
Σ27[1-10](552)	148.4	140	X			
Other GBs						
Σ3[1-10](110)		84	X	X	X	X
Σ5[100](001)		200	X	X	X	X
Σ5[100](013)		62	X	X	X	X
Σ7[11-1](123)		86	X	X	X	X

3.1   Grain boundary energies

3.1.1   Grain boundary energy spectrum for W

The GB energies, γ_{GB}, are shown in Figure 4 for a set of GBs in W for DFT and MEAM. The plot contains all energies of structures identified in the γ-surface approach where the structure of lowest energy always corresponds to the ground state. The energies of the ground state structures depend on the GB character, which has been discussed before, see e.g. Ref. [37]. An important feature in the plot is the low GB energies of the Σ3[1-10](112) tilt GB (0.66 J/m²) and Σ3[1-10](110) twist GB (0.75 J/m²) which arise from the almost bulk like structure of these GBs. All other GB energies are much higher and cluster in the interval from 2 to 2.8 J/m². The highest GB energy is with 3.35 J/m² found for the Σ5[100](001) twist GB.

For every GB, metastable structures were found in addition to the ground state structure. The number of metastable structures correlates with the Σ value which we attribute to the larger GB unit area of

high-Σ GBs and corresponding higher complexity of geometric arrangement. Further, metastable structures exist with an energy very close to the ground state energy for most GBs. This suggests that these structures can be excited at elevated temperatures and, in this way, contribute to the overall behaviour of GBs. We leave a more detailed treatment of such effects to future investigations.

The ground state energies of DFT and MEAM results compare well to each other; the largest differences are seen for the Σ9[1-10](114) and the Σ11[1-10](113) GBs, but still the difference is below 0.3 J/m². DFT and MEAM GB energies compare well for the ground state energies but differ in the excited state energies. The MEAM results seem to cluster at certain energies while energies from DFT calculations are found only at distinct energy levels.
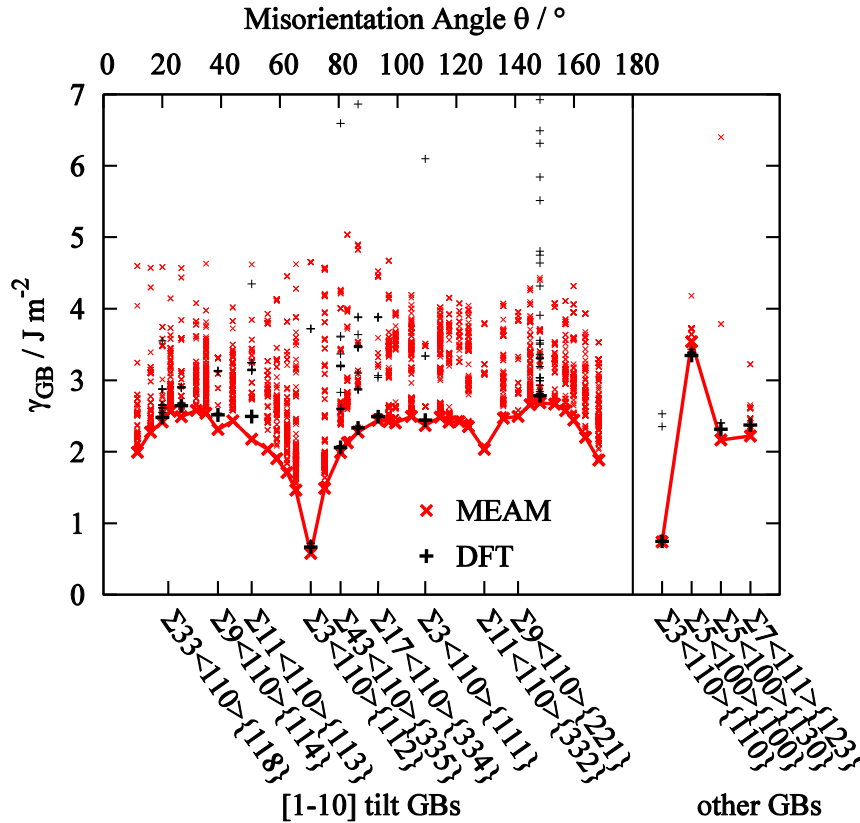

Figure 4: Comparison of γ_{GB} for different GBs in W computed with DFT (black) and once with MEAM potentials (red). Large symbols denote the ground state energy for a GB while smaller symbols are used for exited state energies.

3.1.2 Grain boundary energies for W, Mo, Fe and W25at%Re

We now compare the GB ground state energies for a set of GBs in W, Mo, W25at%Re and Fe between DFT and MEAM in Figure 5. The same trends are found for the anisotropy of the GB energy, however, an offset in the absolute values can be recognized. The highest values are found for W, followed by Mo, W25at%Re and then Fe. As already found for W, the GB of highest energy is the Σ5[100](001) twist GB for all metals. Similarly, the GBs with the lowest energies are again the Σ3[1-10](112) tilt GB and the Σ3[1-10](110) twist GB. The difference between DFT and MEAM is larger for Mo and Fe when comparing to W. For Mo, the MEAM GB energies are about 0.4 J/m² smaller than DFT energies; for Fe, the MEAM GB energies are about 0.5 J/m² smaller than DFT energies. The reasons for these discrepancies will be discussed in Section 3.2 together with the surface energies.

The experimental determination of GB energies is quite challenging, still there exist experimental methods which estimate relative GB energies from triple junctions of GBs [38], or correlate the population of GBs with their energy. In a recent study [39], the distribution of GBs in a slab of ferritic steel was investigated using electron backscatter diffraction (EBSD) and focused ion beam (FIB). From this, the relative population of GBs, i.e. the frequency of occurrence of a specific GB, was determined. In Figure 6, we compare our GB energy data for Fe with these experimental population results. From 0° to 35°, the population decreases in agreement with increasing GB energies. Between 35° and 70°, the opposite trend occurs, followed by a sharp peak of the population at 70°. This peak coincides with the very low GB energy we found for the Σ3[1-10](112) GB. Between 80° and 180°, small features can be recognized for GB energy and population, which are not totally in agreement. Overall in this regime, relatively low populations are observed in agreement with the comparably high GB energies. The good correspondence of DFT and experiment suggest that segregation phenomena in steel do not strongly alter the population when compared to bcc Fe.
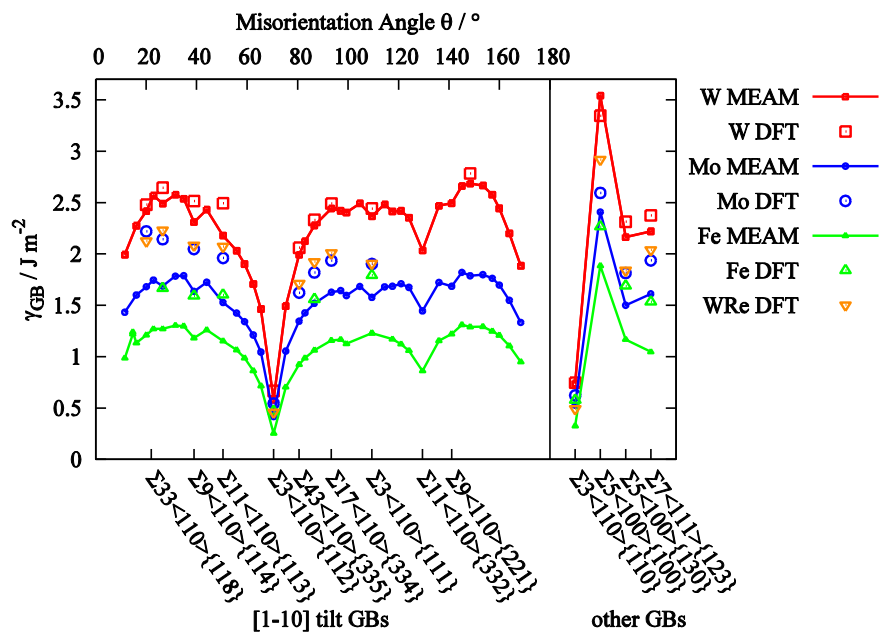

Figure 5: Comparison of γ_{GB} for different GBs in W, Mo, Fe and W25at%Re once computed with DFT (large symbols) and once with MEAM potentials (solid lines).
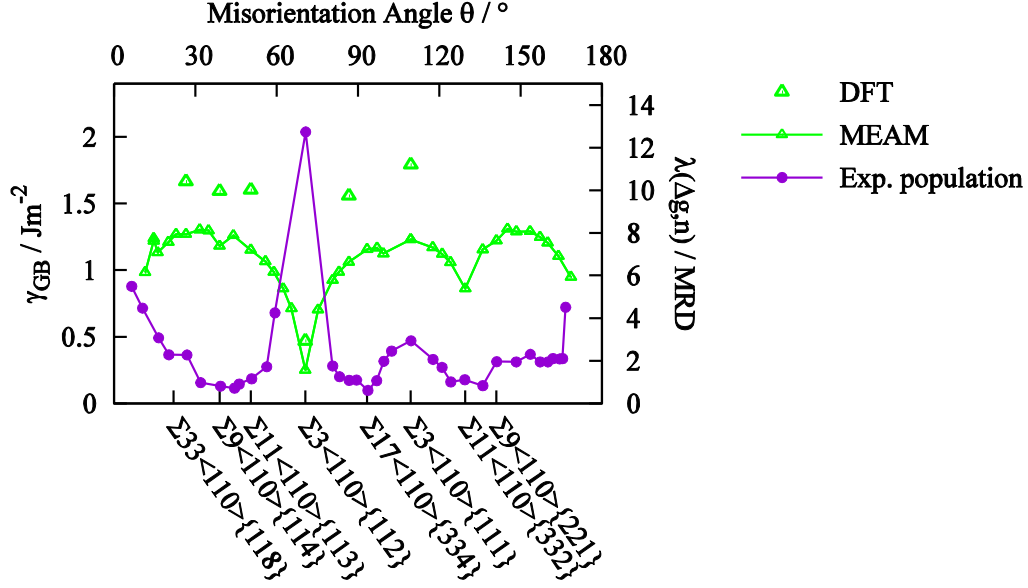
9

Figure 6: Comparison of γ_{GB} from the present DFT and MEAM calculations for Fe (left y-axis) to the population measured by Beladi et al. [39] (Exp.) in ferritic steel (right y-axis) of GBs with a [1-10] misorientation axis. The population of GBs $\lambda(\Delta g, n)$ is given in multiples of the random distribution (MRD).

3.1.3   Ground state structure for the Σ5 grain boundary

Out of all GBs contained in Figure 4, the Σ5[100](013) GB is of particular interest as it has been well characterized both theoretically and experimentally. As summarized in by Ochs et al. [8] results are available for Fe, Nb, Mo, Ta and W. The ground state structure of this GB exhibits an interesting feature: The grains can shift with respect to each other along the [100] direction, breaking mirror symmetry normal to the GB. However, the available results contradict each other for certain elements. We shed more light on this issue by providing a new consistent set of data for DFT and MEAM. We also extend the investigation to V and the W25at%Re alloy.

A side view of the Σ5[100](013) GB is shown in Figure 7 for Mo, where the DFT result (left) is compared to the MEAM result (right). DFT exhibits the shift along the [100] direction in agreement with the experiment (Figure 7.b in Ref. [13]). This can be recognized in the Figure by the lattice planes from the upper grain running exactly between the lattice planes of the lower grain. The shift amounts to 1/4 of the lattice parameter. The MEAM result is in contrast with experiment as the non-shifted structure is identified as the ground state.

The results for all metals are summarized in Table 4, where $\Delta \gamma_{GB} = \gamma_{GB}^{symm} - \gamma_{GB}^{no\ symm}$ gives the difference between the lowest energy structure retaining mirror symmetry and the lowest energy structure which does not. If this quantity is negative, mirror symmetry is energetically preferred and if positive, a structure with broken symmetry is favoured. The table also lists values from literature. Since not always the exact value of $\Delta \gamma_{GB}$ is provided, the reported translation state is denoted by "n" for mirror symmetry and "p" for broken mirror symmetry.

The present DFT data predict a non-symmetric GB structure for all metals with the exception of Ta and Fe, which is in agreement with previous DFT investigations. Larger values of $\Delta \gamma_{GB}$ are observed for Mo, W, W25at%Re and V. For some metals the shift is not exactly 1/4 of the lattice parameter as

for Mo but is in between 1/6 to 1/4 of the lattice parameter. Experiments are not consistent with DFT for Ta and Nb. However, we point out that for these two metals the magnitude of $\Delta\gamma_{GB}$ is moderate.

For MEAM, the gamma surface procedure has not identified the non-symmetric structure as a metastable state for Mo and Nb in contrast to DFT. Hence, the numerical value of $\Delta\gamma_{GB}$ cannot be specified in Table 4. For all other metals both the symmetric and non-symmetric states are metastable. In this case MEAM is in agreement with DFT for W and V and in disagreement for Ta and Fe.
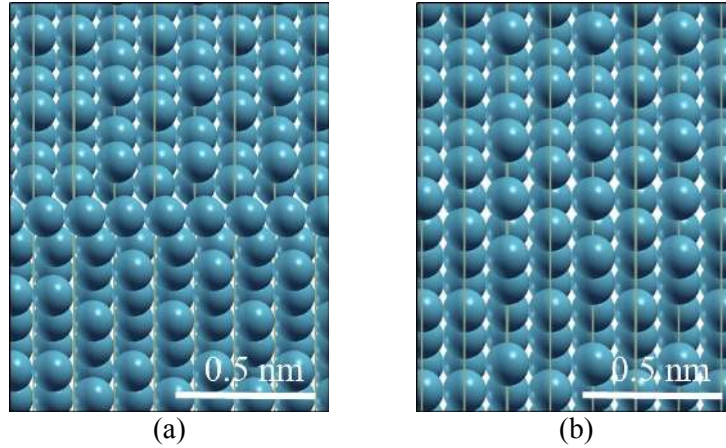

(a)   (b)

Figure 7: Σ5[100](013) structures for Mo viewed from the [013] direction for (a) DFT and (b) MEAM potential.

Table 4: Energy differences for structures with mirror symmetry and without mirror symmetry along the [100] direction for the Σ5 GB in different bcc metals from simulations ($\Delta\gamma_{GB}^{sim}$) and experiments ($\Delta\gamma_{GB}^{exp}$). A positive (negative) value implies that the shifted (non-shifted) structure is energetically more favourable. In case a reference does not provide the value for $\Delta\gamma_{GB}$ but specifies the preference for a shifted or non-shifted GB structure, the information is here included by a "p", or "n", respectively.

Element	$\Delta\gamma_{GB}^{sim}$ / mJ/m²						$\Delta\gamma_{GB}^{exp}$
	DFT	MEAM	DFT	DFT	MGPT	EAM	Exp.
	This work	This work	Ref. [14]	Ref. [8]	Ref. [15]	Ref. [13]	Ref. [13]
Mo	158	n		106	114	p	p
Nb	26	n		8		n	n
Ta	−17	76		n		p	p
W	89	18		100	127		
W25at%Re	47						
V	58	120					
Fe	−2	21	n				

3.1.4 Ground state structures for different grain boundaries

As discussed above, MEAM and DFT predict different ground state structures for the Σ5[100](013) GB. Is this uncertainty unique for this GB or are there GBs with similar problems? In the following, we will compare ground state structures and GB energies for other GBs found by MEAM and DFT to answer this question.

In Figure 8, two possible structures of the Σ19[1-10](116) GB in Mo are shown. The upper structure, which is the ground state structure predicted by MEAM, places two atoms exactly in the GB plane.

The lower structure, the ground state of DFT, reveals a void in the GB plane instead. To address the energetic differences between the two GB structures, the lower structure was also recalculated with MEAM and the upper with DFT. A structural relaxation with adapted lattice parameter was carried out for this purpose. In the case of MEAM, the structural relaxation led only to minor changes in the atomic positions preserving the void. As indicated by the GB energies at the bottom left of the plots (γ_{GB}^{MEAM}), the energy increase with respect to the ground state structure is dramatic for MEAM, i.e. 27%. Hence, the MEAM potential penalizes void formation strongly. For DFT, the structural relaxation of the structure in the upper plot led to significant relaxations, which transformed the structure into one very similar to the DFT ground state: A void is formed again and the energetic difference indicated in the bottom right (γ_{GB}^{DFT}) is much smaller, i.e. about 2%.

We give a similar comparison of GB structures and GB energies from MEAM and DFT in Figure 9 for the Σ17[1-10](334) GB and in Figure 10 for the Σ27[1-10](552) GB, both in W. In this figures, we can see a strong preference of MEAM for symmetric structures in contrast to DFT, which prefers asymmetric structures. Again, the energetic differences between the structures are sizable (see GB energies at the bottom of the plot and Table 5), which shows that the two methods predict different GB ground state structures. Note that the two structures of the Σ27[1-10](552) GB were already presented in previous works [12], [36]. In [36], the structure from Figure 10.a was presented, while in [12] the structure from Figure 10.b was used. Our investigation confirms that the latter is the true DFT ground state, while the former has to be regarded as an excited metastable structure.

As a final aspect we address the question whether computational effort can be saved in the determination of GB ground state structures with a mixed MEAM-DFT approach as has already been employed in e.g. [36]. This implies that the full gamma-surface approach is only carried out with MEAM and the DFT calculation is only repeated for selected structures. From our above investigations of the Σ5, Σ17, Σ19 and Σ27 GBs (summarized in Table 5) we now can distinguish three kinds of error which can result: First, if one only selects the MEAM ground state structure, the correct DFT ground state structure would be missed for all these GBs. Second, if the ground state structure and structures energetically close to it (e.g. within 10% of the GB energy) are taken into account, still for some GBs the DFT ground state structure is missed, (e.g. Σ5, Σ19 in Mo). Third, if all metastable structures from MEAM are recalculated with DFT, yet again for the Σ5[100](013) in Mo the DFT ground state structure would still not be found, as the DFT ground state structure is not a stable structure in MEAM simulations. Hence, a mixed MEAM-DFT approach can lead to erroneous ground state structures for some GBs.
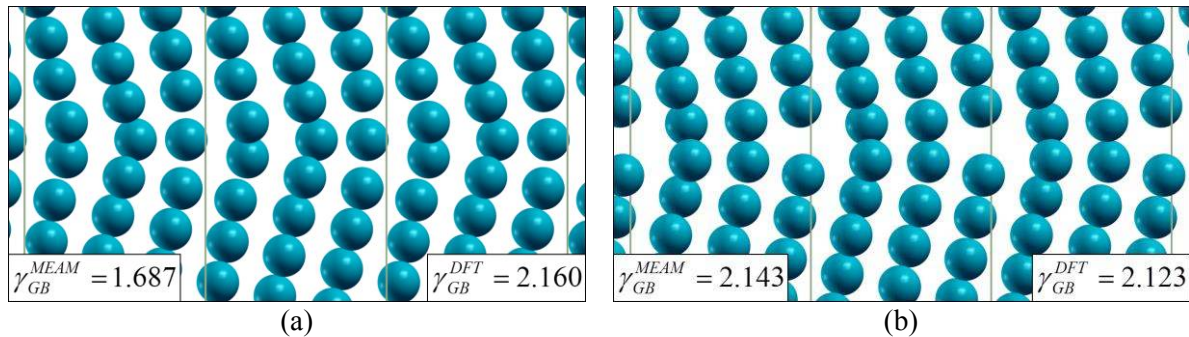

$\gamma_{GB}^{MEAM} = 1.687$ $\gamma_{GB}^{DFT} = 2.160$ $\gamma_{GB}^{MEAM} = 2.143$ $\gamma_{GB}^{DFT} = 2.123$

(a)   (b)

Figure 8: Relaxed ground state structure for the Σ19[1-10](116) GB in Mo from (a) MEAM potential and (b) DFT with GB energy of the structure relaxed with MEAM and with DFT.

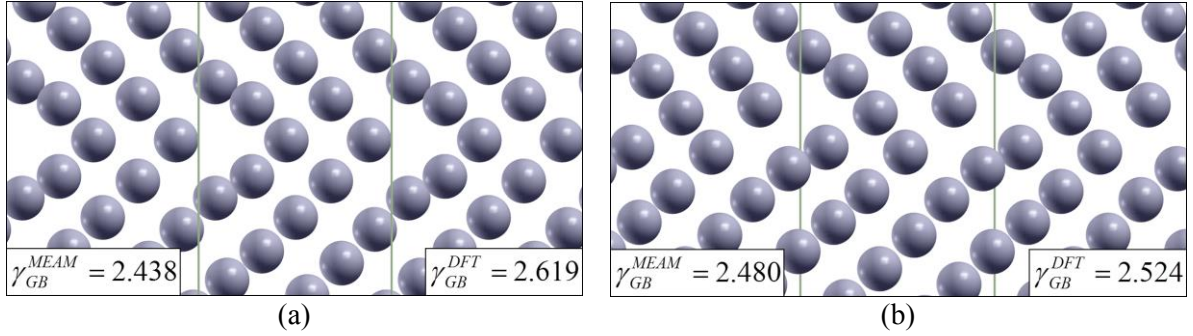$\gamma_{GB}^{MEAM} = 2.438$ $\gamma_{GB}^{DFT} = 2.619$ $\gamma_{GB}^{MEAM} = 2.480$ $\gamma_{GB}^{DFT} = 2.524$

(a)   (b)

Figure 9: Relaxed ground state structure for the Σ17[1-10](334) GB in W from (a) MEAM potential and (b) DFT with GB energy of the structure relaxed with MEAM and with DFT.
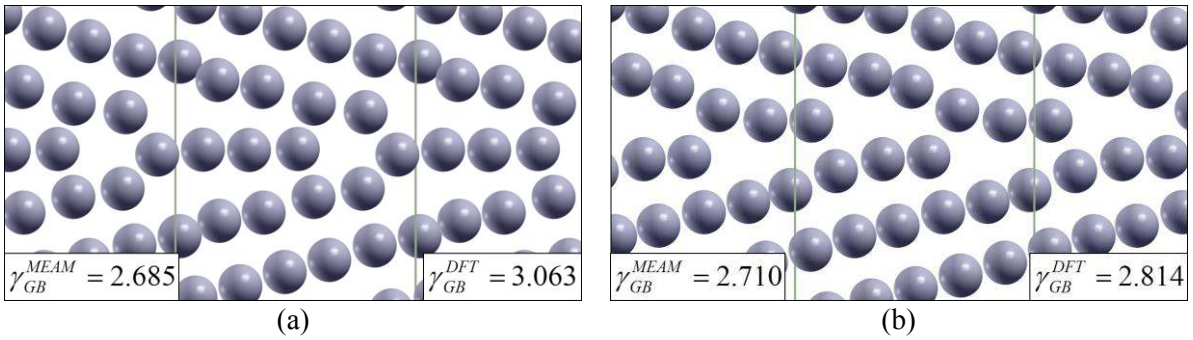

$\gamma_{GB}^{MEAM} = 2.685$ $\gamma_{GB}^{DFT} = 3.063$ $\gamma_{GB}^{MEAM} = 2.710$ $\gamma_{GB}^{DFT} = 2.814$

(a)   (b)

Figure 10: Relaxed ground state structure for the Σ27[1-10](552) GB in W from (a) MEAM potential and (b) DFT with GB energy of the structure relaxed with MEAM and with DFT.

Table 5: Summary of GB ground state energies from MEAM and DFT for selected GBs in W and Mo. $\Delta\gamma_{GB}^{MEAM}$ is the difference in GB energy between two structure a and structure b evaluated by MEAM while $\Delta\gamma_{GB}^{DFT}$ is the same energy difference evaluated with DFT. All quantities are given in J/m².

	Mo			W					
	Σ19[1-10](116)			Σ17[1-10](334)			Σ27[1-10](552)		
	Struct a	Struct b	Δ	Struct a	Struct b	Δ	Struct a	Struct b	Δ
γ_{GB}^{MEAM}	1.687	2.143	-0.456	2.438	2.480	-0.042	2.685	2.710	-0.025
γ_{GB}^{DFT}	2.160	2.123	0.037	2.619	2.524	0.095	3.063	2.814	0.249

3.1.5   Grain boundary excess volume

Due to the disruption of perfect stacking, GBs typically occupy a larger volume than the bulk. The expansion of the GB is quantified by the excess volume which is here denoted by δV. By its definition δV is a one-dimensional quantity, since in GB plane the unit cell dimensions are fixed by the surrounding bulk. [40] Therefore, δV is normalized by the GB area and is given in units of the lattice parameter a_0. We extract δV from the GB calculations as the difference between the distance of the outermost atoms in the GB cell (Figure 2.a) and in the free surface cell (Figure 2.b). The largest value for δV was found for the Σ5[100](001) GB in W for which δV equals to 0.15 a_0 which corresponds to about 0.5 Å. All other GBs reveal smaller values for δV, some even slightly negative. All values are plotted in Figure 11 as a function of γ_{GB} to investigate a correlation of these two quantities. The figure shows a linear relationship between γ_{GB} and δV which reveals that a higher mismatch causes a higher γ_{GB} and also a larger expansion. For W, Mo and W25at%Re the deviation to the linear trend is rather small whereas for Fe the scatter is more pronounced. The slope of the linear fit is very similar for W, Mo and W25at%Re, but differs for Fe which we attribute to the larger scattering and the associated

13

larger uncertainty of the fit. One value, which is particularly off the linear trend, belongs to the $\Sigma5[100](001)$ GB in Fe. It has a negative δV but also the highest γ_{GB} of all GBs treated for Fe. Furthermore, the arithmetic mean values of δV and γ_{GB} are given in Table 6. In general a higher mean in δV implies a higher mean of γ_{GB}. W25at%Re is an exception to this trend since it has a smaller mean of γ_{GB} close to the one of Mo but a mean of δV close to the one of W.

Plots as the one in Figure 11 have already been published in [40], [41] for one bcc metal, Mo, and some fcc metals using semi-empirical potentials. In agreement with our results, they found a strong correlation of δV with the GB energy. For Mo, the values for [100] GBs are in the range of our computations (estimated means: $\delta V \approx 0.1\ a_0$ and $\gamma_{GB} \approx 2$ J/m²) whereas for [1-10] GBs the values are just about half of the magnitude (estimated means: $\delta V \approx 0.035\ a_0$ and $\gamma_{GB} \approx 0.9$ J/m²). No negative values for δV were reported in both studies.

A way to extract δV from experiment is presented in [42], [43], where they measured the GB excess volume of Ni and Cu. In their investigation, they show that the change of volume during recrystallization at a specific temperature range is solely attributed to the release of GB excess volume. In this way they derived for δV the values $0.0909 \pm 0.0104\ a_0$ and $0.0994 \pm 0.0104\ a_0$ for Ni and $0.1274 \pm 0.0305\ a_0$ $0.1274 \pm 0.0305\ a_0$ for Cu. These values are higher than our results for δV (see Table 6), but this can be attributed to a difference between fcc and bcc metals. This would be in accordance with the computations by Yip and Wolf [40], who found larger GB excess volumes for GBs in fcc Cu than in bcc Mo.
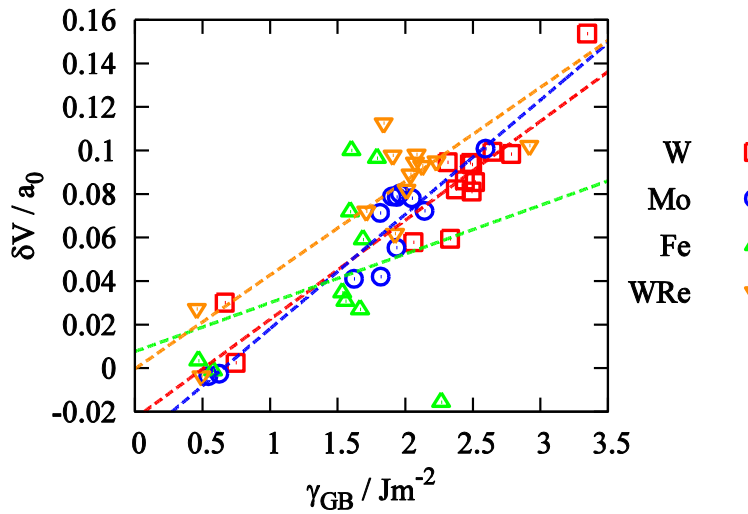

Figure 11: γ_{GB} versus $\delta V/a_0$ for different GBs in W, Mo, Fe and W25at%Re computed with DFT. The dashed lines denote linear fits.

Table 6: Mean δV and γ_{GB} for W, Mo, Fe and W25at%Re.

Element	W	Mo	Fe	W25at%Re
Mean $\delta V/a_0$	0.0786	0.0533	0.0406	0.0799
Mean γ_{GB} / J/m²	2.26	1.78	1.47	1.83

3.2 Surface energies

To access the cohesive properties of GBs, the surfaces created by separating the two grains are essential. The surface energies γ_{FS} of all so formed surfaces are presented in Figure 12. The indices of

the surface are given in the round brackets of the CSL notation in the plot. Compared to γ_{GB}, for which variations were between 20% and 100% of the maximal value, the variations in γ_{FS} are much smaller, only within 80% to 100% of the maximal value. We explain this by the formation of new bonds at the GB which for suitable misorientation can become almost bulk-like. In contrast, atoms at free surfaces loose a similar amount of bonds irrespective of surface orientation.

For all investigated metals, DFT gives the lowest γ_{FS} for the (110) surface. Contrary to that, the surface with the highest γ_{FS} depends on the metal. For W and Mo the (001) surface has the highest γ_{FS} while for Fe the highest γ_{FS} is found for the (111) surface. For W25at%Re the highest γ_{FS} is found for the (118) surface. In comparison to a previous comprehensive overview of DFT surface energies [44], our surface energy values for W and Mo are somewhat smaller, which we attribute to the treatment of surface relaxation in our work. Our values for Fe are higher, since we always used the PBEsol potential, whereas in Ref [44] they used PBE for Fe and LDA for W and Mo.

For all metals, MEAM gives the lowest γ_{FS} for the (110) surface in agreement with DFT. The highest γ_{FS} is never found for the (001) surface: For W it is the (111) surface while for the other metals it is some high-index surface. MEAM was parametrized to give the energetic ordering $\gamma_{FS}^{110} < \gamma_{FS}^{001} < \gamma_{FS}^{111}$ for all bcc transition metals [30], although the experimental justification is only given for Fe [45], [46]. The present investigation reveals that according to DFT, this ordering is correct for Fe but not for W and Mo. Furthermore, DFT and MEAM values reveal a general offset for GB energies. This offset is pronounced for Fe (about 0.6 J/m²) and Mo (about 0.4 J/m²) but smaller for W, where a difference is seen only for some surfaces, especially for the (001) surface. Also the energetic variations appear smaller with MEAM than with DFT in general, which indicates that MEAM underestimates the directional covalent contributions in the bonding of transition metals. Summarizing, there exist important differences for surface energies between MEAM and DFT, which can be expected to also impact the GB calculations.

Comparing surface energies obtained with DFT to experimentally measured values is difficult. Surface energies are measured at high temperatures, while DFT results are valid for 0K. A linear extrapolation formula has to be used to establish a consistent link. The formula proposed by Tyson [47] is used here to extrapolate experimental measurements for W, Mo and Fe from various literature sources to 0K in Table 7. The spread for the extrapolated data on W is quite large ranging from 2 to 6.3 J/m². A trend can be recognized. The lower the measurement temperature, the higher is the surface energy suggesting that a more precise extrapolation procedure should be non-linear. Our results from DFT and MEAM calculations are roughly 4 J/m², i.e. within the experimental range but closer to the low temperature measurements. For Mo and Fe only high-temperature results are available and the spread of the measurements is smaller ranging from 1.8 to 2.8 J/m² for Mo and 2.2 to 2.8 J/m² for Fe. Our values for DFT are not within this interval, which we attribute to the fact that extrapolation from high-temperatures appears to underestimate the experimental surface energies. MEAM is out of the interval for Mo but within the interval for Fe. Since surface energy is a quantity to which MEAMs are fitted, the discrepancy originates from the particular choice of the surface energy in Ref [30].
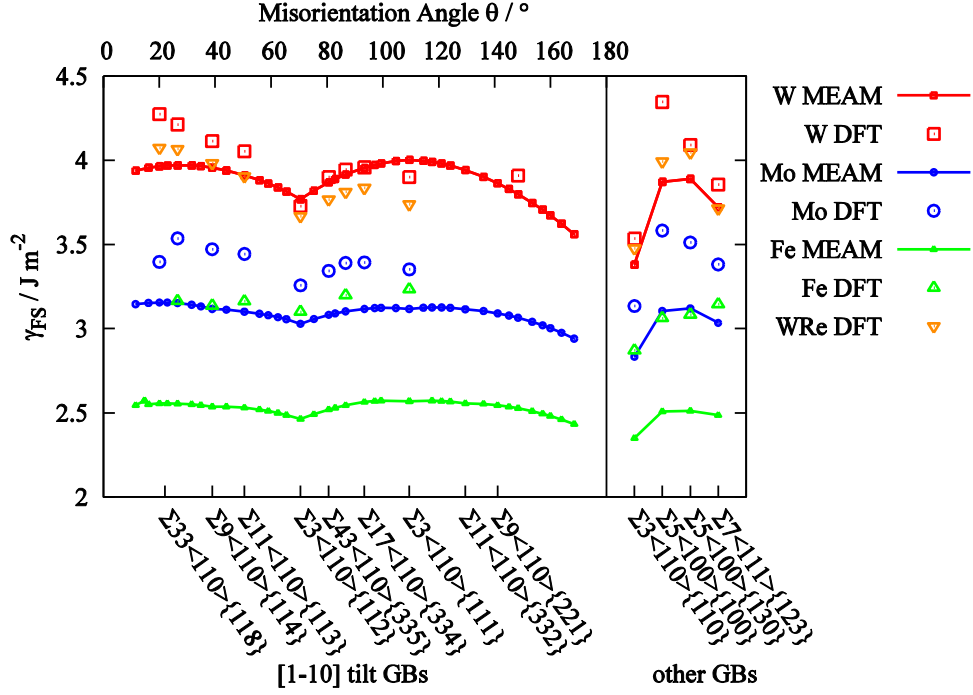
Figure 12: Comparison of γ_{FS} for different GBs in W, Mo, Fe and W25at%Re once computed with DFT (large symbols) and once with MEAM potentials (solid lines).

Table 7: Comparison of experimental surface energies for W and Mo at elevated temperature (γ_{FS}^T / J/m²) as well as extrapolated to 0K (γ_{FS} / J/m²) to our averaged DFT and MEAM results.

W				Mo				Fe			
T [K]	γ_{FS}^T	γ_{FS}	Ref.	T [K]	γ_{FS}^T	γ_{FS}	Ref.	T [K]	γ_{FS}^T	γ_{FS}	Ref.
2000	2.9	3.17	[48]	1700	2.2	2.43	[49]	1733	1.91	2.20	[50]
77	6.3	6.31	[51]	1750	2.6	2.84	[52]	1723	2.09	2.38	[53]
2300	2.8	3.11	[54]	2623	1.96	2.32	[55]	1713	2.03	2.31	[56]
2273	1.68	1.99	[57]	1873	2.11	2.37	[55]	1683	2.41	2.69	[58]
1773	2.83	3.07	[59]	2773	1.9	2.28	[60]	1753	2.53	2.82	[61]
1573	4.5	4.71	[62]	1773	2.05	2.29	[59]				
2273	1.81	2.12	[63]	2673	1.39	1.76	[63]				
				2773	1.86	2.25	[63]				
				1873	1.75	2.01	[63]				
0		3.99	DFT	0		3.40	DFT	0		3.12	DFT
0		3.87	MEAM	0		3.09	MEAM	0		2.53	MEAM

3.3 Work of separation

The work of separation is an important indicator for the cohesive strength of GBs. It is computed with Eq. 2.3, which requires the GB energy γ_{GB} and the free surface energy γ_{FS}. In Figure 13 the work of separation is shown for the GBs investigated. Again, a strong anisotropy is observable, where the Σ3[1-10](112) tilt GB exhibits the highest work of separation for every metal and both DFT and MEAM. The Σ5[100](001) twist GB exhibits the lowest W_{sep} for every metal when calculated with MEAM and for Mo, W25at%Re and Fe when treated with DFT. For W, DFT predicts the W_{sep} of the Σ5[100](001) to be among the smallest values, but the smallest value of W_{sep} is found for the Σ27[1-10](552) tilt GB, which has not been computed for the other metals. Comparing DFT and MEAM

results gives similar deviations as before: for W about 0.1 J/m² on average, with a larger deviation for the Σ5 twist GB, for Mo 0.4 J/m² and for Fe 0.6 J/m².

The work of separation can also be compared to experimental data. According to Griffith theory, there exists the following relationship to the fracture stress, see also [64]:

$$\sigma_f \propto W_{sep} + \gamma_p \qquad\qquad 3.1$$

In this equation, σ_f denotes the fracture stress and γ_p is the plastic contribution to the fracture. According to [65], [66], the plastic contribution γ_p is proportional to W_{sep}, which finally leads to $\sigma_f \propto W_{sep}$. There is published data on the fracture stress of GBs in Mo and a comparison of their measurements to our data is given in Figure 14. Note that the data of Brosse et al. [67] has been obtained at room temperature, while the data from Kurishita et al. [68] and Tsurekawa et al. [64] was taken at 77 K.

Our calculations agree well with the fracture stresses measurements from Kurishita et al. Also the results from Brosse et al. correspond to spikes in our calculations. The data from Tsurekawa et al. shows larger discrepancies and further, their data is also in contrast to the data from Brosse. The direct comparison of the experimental data to each other or to our results has to be made with caution, because the experiments were performed at different temperatures and we cannot estimate the influence of impurities at the experimental measurement. The impurities may be the reason for the much lower fracture stresses that have been measured by Brosse in contrast to the data from Kurishita and Tsurekawa.
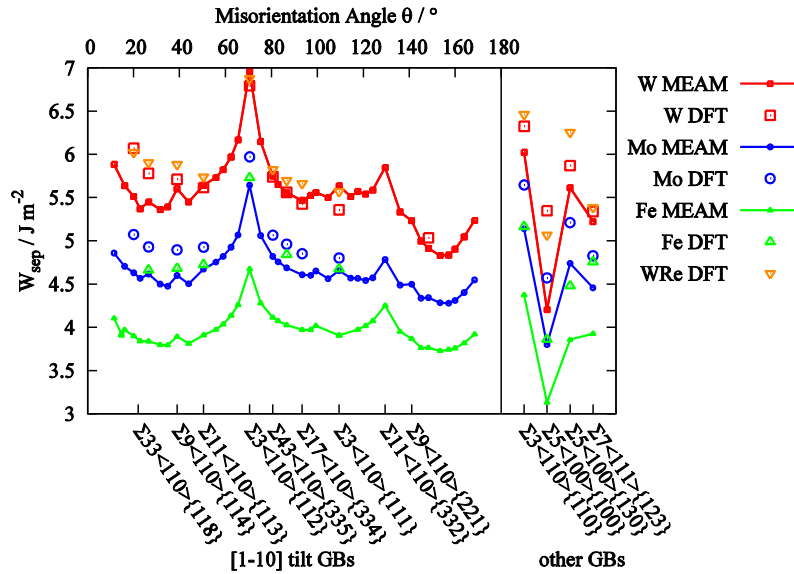

Figure 13: Comparison of W_{sep} for different GBs in W, Mo, Fe and W25at%Re once computed with DFT (large symbols) and once with MEAM potentials (solid lines).
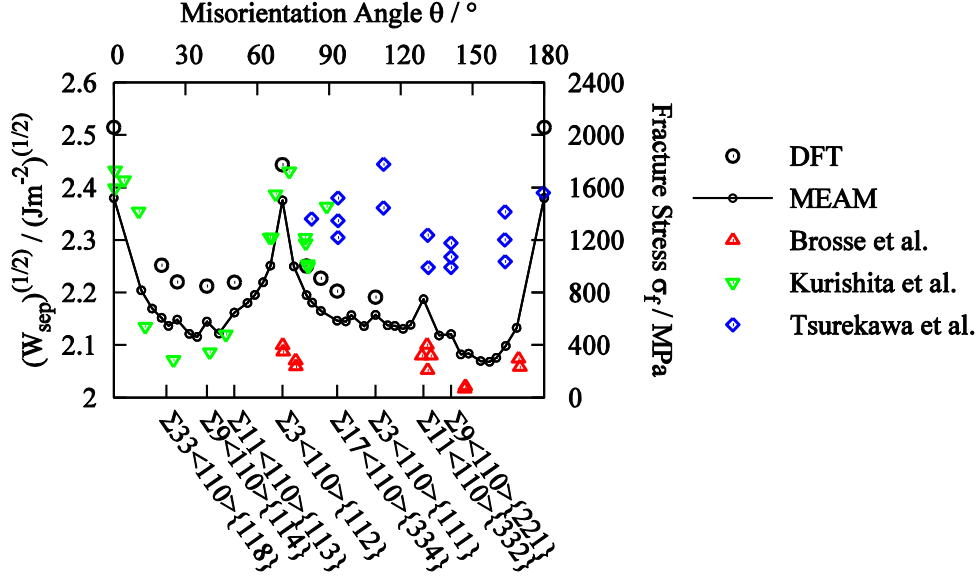
Figure 14: Comparison of $(W_{sep})^{\frac{1}{2}}$ from our DFT and MEAM calculations to the fracture stress measured in experiments by Brosse et al. [67] at room temperature, and Kurishita et al. [68] and Tsurekawa et al. [64] at 77K for [1-10] tilt GBs.

3.4   Transgranular versus intergranular fracture

A fundamental property of bcc transition metals is the transition from ductile to brittle fracture at a specific temperature which depends on the metal. In the brittle regime some metals fail by cleavage through the grain (transgranular fracture) while others fail by crack propagation along GBs (intergranular fracture). From work of separation and free surface energies, we can evaluate the tendency for intergranular or transgranular fracture in the brittle regime. In [69], the ratio

$$R = \frac{W_{sep}}{2\,\gamma_{FS}^{PCP}}$$

(3.2)

is defined, where γ_{FS}^{PCP} denotes the surface energy of the preferred cleavage plane. For bcc metals, this is mainly the [100] plane [70], [71]. If R is close to unity, transgranular cleavage is preferred, while for lower values intergranular fracture is expected.

We have evaluated R from the DFT results in W, Mo, Fe and W25at%Re. For each metal the arithmetic mean of *R* for all GBs is shown in Figure 15. The value of R is lowest for W followed by Mo, WRe and Fe. This strongly correlates with the position of the (100) surface energy in Figure 12. For W the (100) surface has the highest surface energy while for Mo, WRe and Fe the (100) surface energy decreases relative to the energies of the other surfaces. The MEAM result of R for the bcc transition metals V, Nb, Ta, Cr, Mo, W and Fe is also shown in Figure 15. The trend observed for DFT is reproduced with a small offset in R of about 0.05. Further, all the metals not considered by DFT reveal rather large R values comparable with the ones obtained for Fe.

Our findings for R are in accordance with experiments [70], [72], [73], which show a preferred transgranular fracture for V, Nb, Ta, Cr and Fe, while Mo and W exhibit mainly intergranular fracture in the brittle fracture regime.
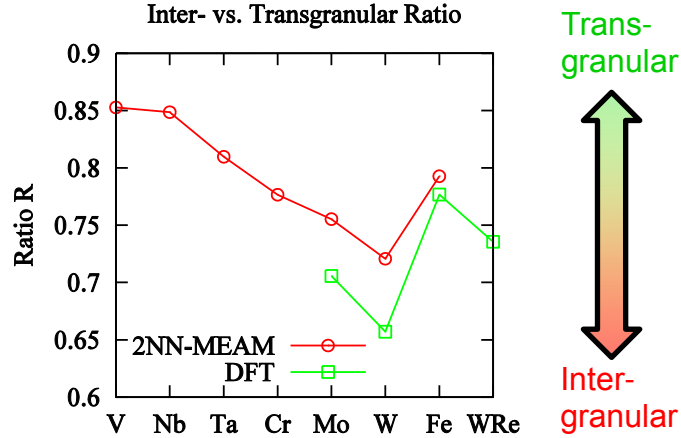
Figure 15: Comparing R for all GBs for MEAM potentials and DFT.

4   Conclusion

In this study, we presented GB properties for a large set of GBs in bcc transition metals. The four metals W, Mo, Fe and the W25at%Re alloy were treated with DFT while the somewhat larger set of metals W, Mo, Fe, V, Nb, Ta, Cr were treated with semi-empirical 2NN MEAM potentials. First, we conducted a DFT convergence study and compared three different simulation setups. With the optimal settings we carried out a systematic search for the ground state structure for each GB based on a γ−surface approach. For the obtained ground state structure we computed GB energies, surface energies, work of separation, GB excess volume and the tendency for intergranular or transgranular fracture.

We find that for every GB several metastable structures exist in addition to the ground state. While for low Σ GBs the energy difference between ground state and exited states is substantial, for high Σ GBs the difference can be quite small indicating that such exited states might also be relevant for the properties of these GBs. The GB energies exhibit a strong dependency on misorientation angle and, as a general trend, the largest values are found for W, followed by W25at%Re, Mo and Fe. Comparison of the different GB properties was made to experimental surface energies, experimental GB distribution, experimental fracture stress and experimental excess volumes. Overall reasonable agreement was found. In particular, based on a simple criterion we can reproduce the experimentally observed tendency for increased intergranular failure for W and Mo which we trace down to their high (100) surface energy.

The comparison of ground state structure obtained from DFT and MEAM revealed significant differences for some GBs. We discussed in detail the $\Sigma5[100](013)$ GB where the direct comparison to experimental values showed that DFT predicts the correct ground state, while the MEAM potential does not. Similarly also for other GBs, e.g. $\Sigma19[1\text{-}10](116)$ in Mo, $\Sigma17[1\text{-}10](334)$ and $\Sigma27[1\text{-}10](552)$ in W, differences exist. Also, MEAM underestimates GB energies especially for Fe and Mo while for W the agreement is satisfactory. Despite these discrepancies the dependency of GB energies with misorientation and also the ratio R for inter- or transgranular fracture is reproduced well.

Appendix

Appendix A   Convergence study

Several parameters have to be checked before starting a DFT simulation. These parameters include the k-Point mesh, the energy cut-off, which algorithm to use for the ionic relaxation and the convergence criterion for the ionic relaxation. Another parameter that is system specific is the vacuum thickness, which is the amount of vacuum between two free surfaces that is necessary to exclude interactions. All convergence tests were performed for the $\Sigma3[1\text{-}10](111)$ tilt GB in W. The target accuracy is a maximum deviation of 1% of the property value.

A.1   k-points and energy cut-off

Two important parameters for the accuracy of the results are the number of k-points and the energy cut-off used for the calculations. To compare and work with results from different configurations, the k-point sampling, the energy cut-off and the simulation cell size should be the same to exclude side effects. We first show the convergence of the total energy with respect to the k-point sampling in Figure A1 for different structures that are given in Figure 1 (GB, free surface and bulk structure). The cell dimensions for all these structures are 4.47 x 4.47 x z Å, where z can vary. The number of k-points N used in x- and y-direction is the same whereas a smaller number N_z is used in z-dimension because of the larger elongation in this direction. From the figure we observe that for GB and bulk configuration a 7 x 7 x 1 and for the free surface configuration 5 x 5 x 1 k-point sampling is sufficient. While we find that one k-point in z-direction is enough for GB and free surface structures with a grain thickness of 22Å, the bulk configuration needs more than one k-point in z-direction if the total length of the cell is below 65Å.

The number of plane waves used in the calculations is controlled by the energy cut-off parameter. A default energy cut-off is supplied by the pseudopotentials provided by VASP, but should be checked nevertheless. The parameter has been examined for GB structures without and with vacuum on top (Figure 1.a and Figure 2.a) and a 22 Å grain thickness. The GB properties γ_{GB}, γ_{FS} and W_{sep} are computed using equations 2.1-2.3 without ionic relaxation. In Figure A2 the GB properties are presented for different energy cut-offs (default value: $E_{cutoff} = 223$ eV). We observe that for configurations with and without vacuum the default energy cut-off can be used. A larger energy cut-off of $E_{cutoff} = 400$ eV is needed for the setup making use of the cell relaxation (see Appendix C).
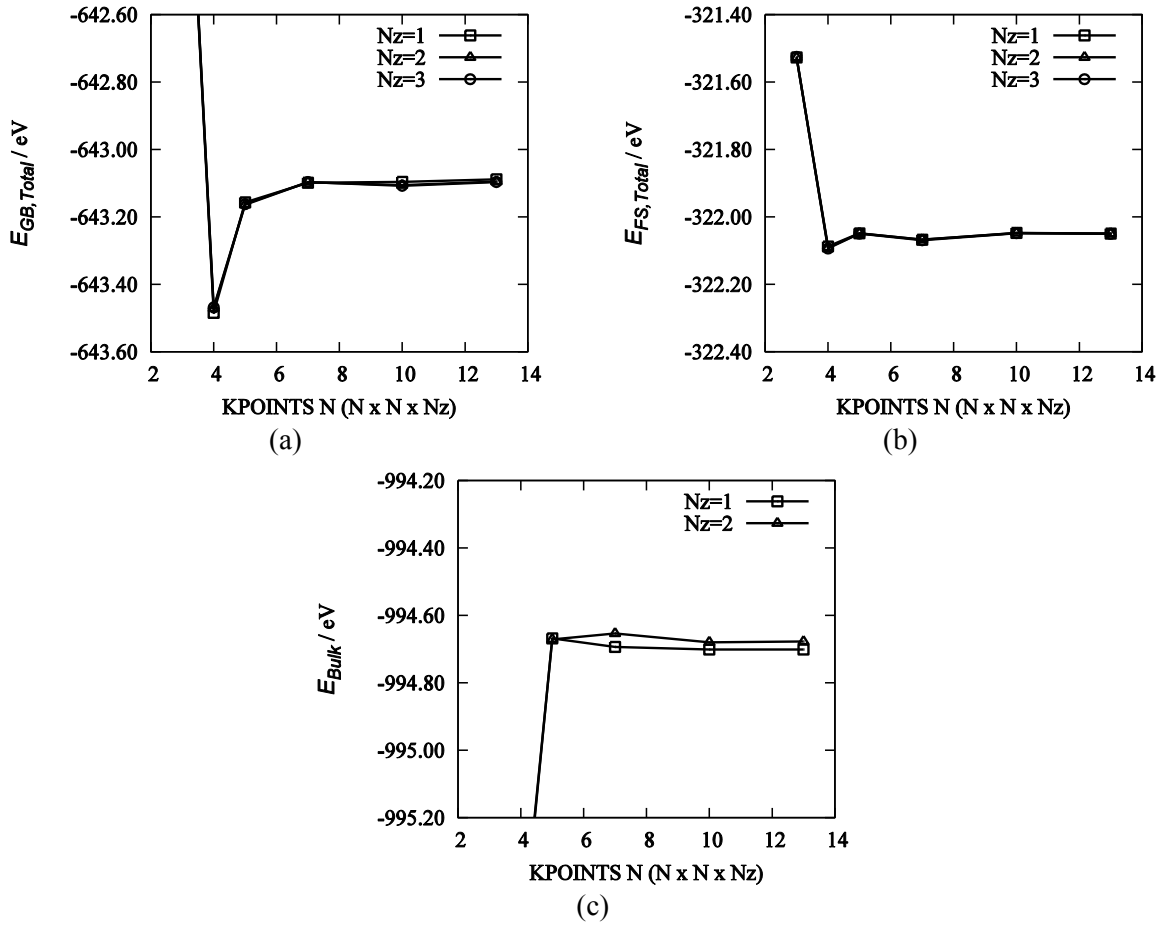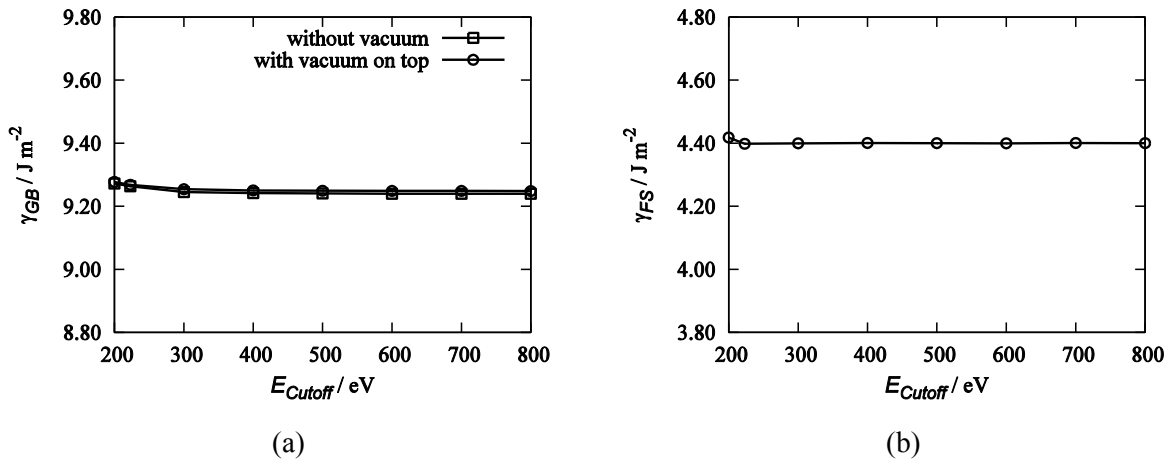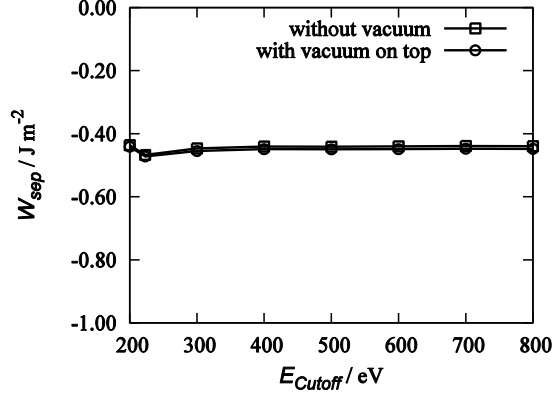
Figure A1: k-point convergence for (a) GB, (b) free surface and (c) bulk structure. Grain thickness for GB and free surface was 22Å (cell length: 44Å), the bulk cell was 65Å long.

(c)

Figure A2: Convergence of (a) γ_{GB}, (b) γ_{FS} and (c) W_{sep} with respect to the energy cutoff.

A.2 Vacuum thickness

This convergence test regards the vacuum thickness that is needed to exclude interaction effects of the free surfaces. For that purpose, we converge the surface energy with respect to the vacuum thickness between two surfaces, which is presented in Figure A3. We see that the effects on the free surface energy vanish for 6Å of vacuum and more in the cell.
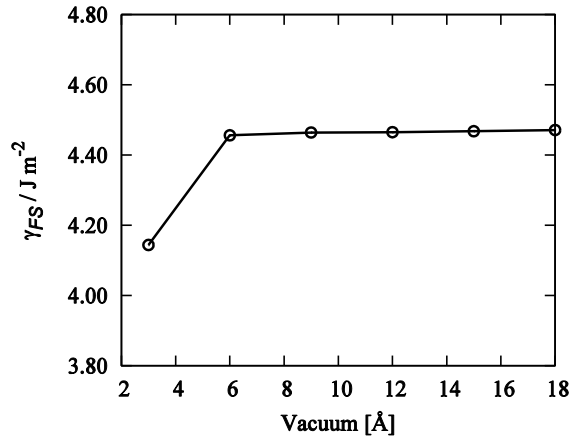

Figure A3: Convergence of γ_{FS} with respect to the vacuum thickness.

## Appendix B Exchange-correlation potential

To decide which exchange correlation functional will be used for the simulations, we calculate the lattice constant and the bulk modulus for a set of functionals, as there are LDA [74], PBE [75], [76], AM05 [77], [78] and PBEsol [27], and compare the results to experimental measurements. The lattice constant and the bulk modulus are obtained by fitting the energy per atom in a bcc structure computed for different trial lattice constants with the Birch-Murnaghan equation of state (see Figure B1 for PBEsol). From this fitting procedure, the bulk modulus and the lattice constant are then easily computed. We compare the lattice constants obtained with different functionals to experimental observations in Table B1.

The lattice constant and the bulk modulus are best estimated by PBEsol; also PBEsol has been introduced to improve the performance of PBE for solids and has been shown to predict equilibrium properties in general more accurately [27]. For this reason and the good agreement with the

22

experimental value the following convergence studies will make use of the PBEsol-functional if not explicitly mentioned otherwise.

Another method to obtain the lattice constant is to use of the cell relaxation algorithm of VASP. From a starting lattice constant, VASP calculates the stress and optimizes the cell according to it, afterwards the lattice constant can be computed from the optimized cell. For this method, we converge the lattice constant with respect to the energy cut-off. By that, we obtain the same result as for the Birch-Murnaghan fit, see Figure B1. In addition, this figure shows that an energy cut-off of 400 eV is needed for reliable results when the cell relaxation algorithm is applied.

We then compute the work of separation, the GB energy and the free surface energy with different xc-functionals and the corresponding lattice constants from Table B1. A comparison of the different obtained values is given in Table B2. No values are given for the AM05-functional as the calculations failed to converge for the configurations containing free surfaces or a GB. From the table, we see that LDA compares very well to PBEsol in contrast to PBE, which gives the lowest values for all three quantities of interest. An important finding is that compared to other parameters tested in the convergence section the choice of the xc-functional results in the largest deviations.
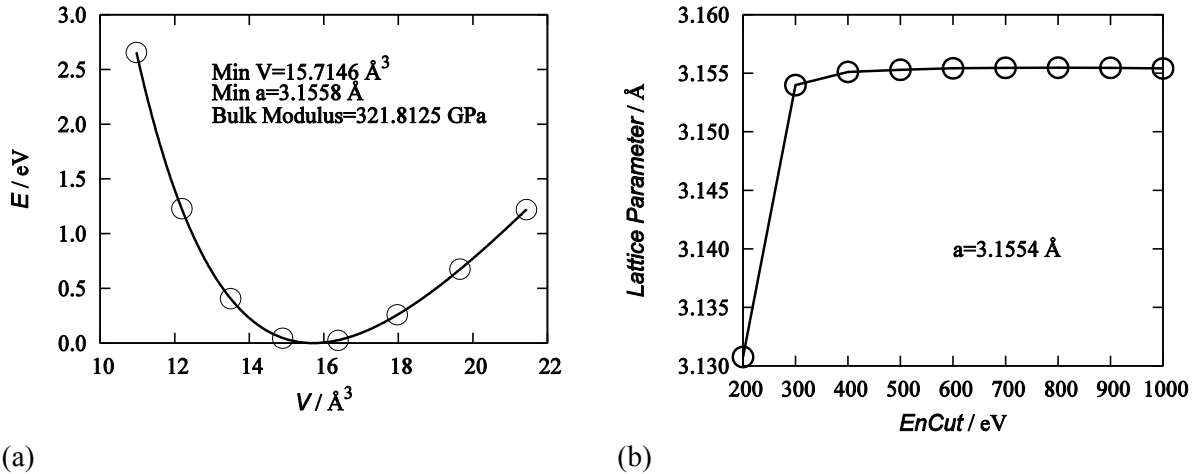
(a)　　　　　　　　　　　　　　　　　　　　　　　(b)

Figure B1: Calculation of the lattice constant via Birch-Murnaghan fit (left) and cell relaxation (right) for PBEsol.

Table B1: Comparison of the lattice constant calculated with different xc-functionals to experimental data [79].

xc-Functional	Lattice Constant / Å	Bulk Modulus / GPa
LDA	3.1405	332.0
PBE	3.1855	301.3
PBEsol	3.1558	321.8
AM05	3.1499	324.0
Exp.	3.1651	314.2

Table B2: Comparison of GB properties for the $\Sigma3[1\text{-}10](111)$ GB in W evaluated with different xc-potentials. All energies are given in J/m².

xc-Functional	γ_{GB}	γ_{FS}	W_{sep}
LDA	2.403	3.928	5.453
PBE	2.271	3.528	4.785
PBEsol	2.418	3.881	5.343

Appendix C   DFT and MEAM lattice constants for bcc transition metals

To calculate GB properties for different elements, the lattice constant for the used potential has to be determined. As described in Appendix B, the lattice constant and bulk modulus for a set of elements are computed from a fit of the Birch-Murnaghan equation of state to energies from cells with different lattice parameters. Table C1 lists the resulting values for the PBEsol exchange correlation potential and the semi-empirical MEAM potential.

Table C1: Lattice constant a_0 calculated with the PBEsol xc-potential and MEAM potential for different elements as well as experimental values.

Element	Source	a_0 / Å	Bulk Modulus / GPa
W	DFT	3.1558	321.8
	MEAM	3.1639	313.2
	Exp. [79]	3.1651	314.2
W25at%Re	DFT	3.1345	341.2
	MEAM	-	-
	Exp.	-	-
Ta	DFT	3.2823	207.4
	MEAM	3.3024	192.1
	Exp. [80]	3.296	197.2
Mo	DFT	3.1292	278.2
	MEAM	3.1464	263.3
	Exp. [79]	3.1468	265.3
Nb	DFT	3.2833	186.5
	MEAM	3.3024	171.6
	Exp. [80]	3.301	170.4
Fe	DFT	2.7915	204.3
	MEAM	2.8636	171.8
	Exp.[81]	2.8665	171.8
V	DFT	2.9613	194.8
	MEAM	3.0310	156.1
	Exp. [80]	3.024	157.3

References

[1]   W. Setyawan and R. J. Kurtz, "Effects of transition metals on the grain boundary cohesion in tungsten," *Scr. Mater.*, vol. 66, p. 558, 2012.

[2]   G. H. Campbell, J. Belak, and J. a Moriarty, "Atomic structure of the Σ5 (310)/[001] symmetric tilt grain boundary in tantalum," *Scr. Mater.*, vol. 43, no. 7, pp. 659–664, Sep. 2000.

[3]   J.-M. Zhang, F. Maa, and K.-W. Xu, "Calculation of the surface energy of FCC metals with modified embedded-atom method," *Appl. Surf. Sci.*, vol. 229, p. 34, 2004.

[4]   H.-K. Kim, W.-S. Ko, H.-J. Lee, S. G. Kim, and B.-J. Lee, "An identification scheme of grain boundaries and construction of a grain boundary energy database," *Scr. Mater.*, vol. 64, no. 12, pp. 1152–1155, Jun. 2011.

[5]   B.-J. Lee, W.-S. Ko, H.-K. Kim, and E.-H. Kim, "The modified embedded-atom method interatomic potentials and recent progress in atomistic simulations," *Calphad*, vol. 34, no. 4, pp. 510–522, Dec. 2010.

[6]   H. Hurchand, S. D. Kenny, and R. Smith, "The interaction of P atoms and radiation defects with grain boundaries in an α-Fe matrix," *Nucl. Instruments Methods Phys. Res. Sect. B Beam Interact. with Mater. Atoms*, vol. 228, no. 1–4, pp. 146–150, Jan. 2005.

[7]   W.-S. Ko, J. B. Jeon, C.-H. Lee, J.-K. Lee, and B.-J. Lee, "Intergranular embrittlement of iron by phosphorus segregation: an atomistic simulation," *Model. Simul. Mater. Sci. Eng.*, vol. 21, no. 2, p. 25012, Mar. 2013.

[8]   T. Ochs, O. Beck, C. Elsässer, and B. Meyer, "Symmetrical tilt grain boundaries in body-centred cubic transition metals: An ab initio local-density-functional study," *Philos. Mag. A*, vol. 80, no. 2, pp. 351–372, Feb. 2000.

[9]   M. Mrovec, T. Ochs, V. Vitek, D. Nguyen-manh, and D. G. Pettifor, "Never ending saga of a simple boundary," *Zeitschrift für Met.*, vol. 94, pp. 1–6, 2003.

[10]   A. Y. Lozovoi, A. T. Paxton, and M. W. Finnis, "Structural and chemical embrittlement of grain boundaries by impurities: A general theory and first-principles calculations for copper," *Phys. Rev. B*, vol. 74, p. 155416, 2006.

[11]   E. Wachowicz and A. Kiejna, "Effect of impurities on structural, cohesive and magnetic properties of grain boundaries in α -Fe," *Model. Simul. Mater. Sci. Eng.*, vol. 19, no. 2, pp. 1–20, Mar. 2011.

[12]   W. Setyawan and R. J. Kurtz, "Ab initio study of H, He, Li and Be impurity effect in tungsten Σ3{1 1 2} and Σ27{5 5 2} grain boundaries," *J. Phys. Condens. Matter*, vol. 26, no. 13, p. 135004, 2014.

[13]   G. H. Campbell, M. Kumar, W. E. King, J. Belak, J. a. Moriarty, and S. M. Foiles, "The rigid-body displacement observed at the ∑ = 5, (310)-[001] symmetric tilt grain boundary in central transition bcc metals," *Philos. Mag. A*, vol. 82, no. 8, pp. 1573–1594, May 2002.

[14]   M. Čák, M. Šob, and J. Hafner, "First-principles study of magnetism at grain boundaries in iron and nickel," *Phys. Rev. B*, vol. 78, no. 5, p. 54418, Aug. 2008.

[15] A. G. Marinopoulos, V. Vitek, and A. E. Carlsson, "Significance of non-central forces in atomistic studies of grain boundaries in bcc transition metals," *Philos. Mag. A*, vol. 72, no. 5, pp. 1311–1330, 1995.

[16] L. Nordheim, "Zur Elektronentheorie der Metalle," *Ann. Phys.*, vol. 401, pp. 607–640, 1931.

[17] J. S. S. Faulkner, "The modern theory of alloys," *Prog. Mater. Sci.*, vol. 27, no. 1–2, pp. 1–187, Jan. 1982.

[18] D. Scheiber, V. I. Razumovskiy, P. Puschnig, R. Pippan, and L. Romaner, "Ab initio description of segregation and cohesion of grain boundaries in W–25at.% Re alloys," *Acta Mater.*, vol. 88, no. 0, pp. 180–189, 2015.

[19] G. Kresse and J. Hafner, "Ab initio molecule dynamics for liquid metals," *Phys. Rev. B*, vol. 47, p. 558, 1993.

[20] G. Kresse and J. Hafner, "Ab initio molecular-dynamics simulation of the liquid-metal-amorphous-semiconductor transistion in germanium," *Phys. Rev. B*, vol. 49, p. 14251, 1994.

[21] G. Kresse and J. Hafner, "Norm-conserving and ultrasoft pseudopotentials for first-row and transition-elements," *J. Phys. Condens. Matter*, vol. 6, p. 8245, 1994.

[22] G. Kresse and J. Furthmüller, "Efficiency of ab-initio total energy calculations for metals and semiconductors using a plane-wave basis set," *Comput. Mater. Sci.*, vol. 6, pp. 15–20, 1996.

[23] G. Kresse and J. Furthmüller, "Efficient iterative schemes for ab initio total-energy calculations using a plane-wave basis set," *Phys. Rev. B*, vol. 54, p. 11169, 1996.

[24] D. Vanderbilt, "Soft self-consistent pseudopotentials in a generalized eigenvalue formalism," *Phys. Rev. B*, vol. 41, p. 7892, 1990.

[25] P. E. Blöchl, "Projector augmented-wave method," *Phys. Rev. B*, vol. 50, p. 17953, 1994.

[26] G. Kresse and D. Joubert, "From ultrasoft pseudopotentials to the projector augmented-wave method," *Phys. Rev. B*, vol. 59, p. 1758, 1999.

[27] J. P. Perdew, A. Ruzsinszky, G. I. Csonka, O. A. Vydrov, G. E. Scuseria, L. A. Constantin, X. Zhou, and K. Burke, "Restoring the Density-Gradient Expansion for Exchange in Solids and Surfaces," *Phys. Rev. Lett.*, vol. 100, no. 13, p. 136406, 2008.

[28] L. Romaner, C. Ambrosch-Draxl, and R. Pippan, "Effect of Rhenium on the Dislocation Core Structure in Tungsten," *Phys. Rev. Lett.*, vol. 104, p. 195503, 2010.

[29] H. Li, S. Wurster, C. Motz, L. Romaner, C. Ambrosch-Draxl, and R. Pippan, "Dislocation-core symmetry and slip planes in tungsten alloys: Ab initio calculations and microcantilever bending experiments," *Acta Mater.*, vol. 60, p. 748, 2012.

[30] B.-J. Lee, M. I. I. Baskes, H. Kim, and Y. Koo Cho, "Second nearest-neighbor modified embedded atom method potentials for bcc transition metals," *Phys. Rev. B*, vol. 64, no. 18, p. 184102, Oct. 2001.

[31] S. Plimpton, "Fast Parallel Algorithms for Short-Range Molecular Dynamics," *J. Comput. Phys.*, vol. 117, p. 1, 1995.

[32] "http://lammps.sandia.gov." .

[33] S. R. Bahn and K. W. Jacobsen, "An object-oriented scripting interface to a legacy electronic structure code," *Comput. Sci. Eng.*, vol. 4, no. 3, pp. 56–66, 2002.

[34] G. I. Csonka, J. P. Perdew, A. Ruzsinszky, P. H. T. Philipsen, S. Lebegue, J. Paier, O. A. Vydrov, and J. G. Angyan, "Assessing the performance of recent density functionals for bulk solids," *Phys. Rev. B*, vol. 79, no. 15, p. 155107, 2009.

[35] J. R. Rice and R. Thomson, "Ductile versus Brittle Behavior of Crystals," *Phil. Mag.*, vol. 29, no. 1, pp. 73–97, 1974.

[36] W. Setyawan and R. J. Kurtz, "Effects of transition metals on the grain boundary cohesion in tungsten," *Scr. Mater.*, vol. 66, no. 8, p. 558, 2012.

[37] D. Wolf, "Correlation between the energy and structure of grain boundaries in b.c.c. metals: II. Symmetrical tilt boundaries," *Philos. Mag. A*, vol. 62, no. 4, pp. 447–464, 1990.

[38] S. J. Dillon and G. S. Rohrer, "Characterization of the Grain-Boundary Character and Energy Distributions of Yttria using Automated Serial Sectioning and EBSD in the FIB," *J. Am. Ceram. Soc.*, vol. 92, no. 7, pp. 1580–1585, Jul. 2009.

[39] H. Beladi and G. S. Rohrer, "The relative grain boundary area and energy distributions in a ferritic steel determined from three-dimensional electron backscatter diffraction maps," *Acta Mater.*, vol. 61, no. 4, pp. 1404–1412, Feb. 2013.

[40] S. Yip and D. Wolf, "Atomistic Concepts for Simulation of Grain Boundary Fracture," in *Grain Boundary Chemistry and Intergranular Fracture*, 1991, vol. 46, pp. 77–168.

[41] D. L. Olmsted, S. M. Foiles, and E. a. Holm, "Survey of computed grain boundary properties in face-centered cubic metals: I. Grain boundary energy," *Acta Mater.*, vol. 57, no. 13, pp. 3694–3703, Aug. 2009.

[42] E.-M. Steyskal, B. Oberdorfer, W. Sprengel, M. Zehetbauer, R. Pippan, and R. Würschum, "Direct Experimental Determination of Grain Boundary Excess Volume in Metals," *Phys. Rev. Lett.*, vol. 108, no. 5, p. 55504, Jan. 2012.

[43] B. Oberdorfer, D. Setman, E.-M. Steyskal, A. Hohenwarter, W. Sprengel, M. Zehetbauer, R. Pippan, and R. Würschum, "Grain boundary excess volume and defect annealing of copper after high-pressure torsion," *Acta Mater.*, vol. 68, no. 0, pp. 189–195, 2014.

[44] L. Vitos, A. V Ruban, H. L. Skriver, J. Kolla, and J. Kollar, "The surface energy of metals," *Surf. Sci.*, vol. 411, pp. 186–202, 1998.

[45] H. E. Grenga and R. Kumar, "Surface energy anisotropy of iron," *Surf. Sci.*, vol. 61, no. 1, pp. 283–290, 1976.

[46] B. E. Sundquist, "A direct determination of the anisotropy of the surface free energy of solid gold, silver, copper, nickel, and alpha and gamma iron," *Acta Metall.*, vol. 12, no. 1, pp. 67–86, Jan. 1964.

[47] W. R. Tyson, "Surface energies of solid metals," *Can. Metall. Q.*, vol. 14, no. 4, pp. 307–314, 1975.

[48] J. P. Barbour, F. M. Charbonnier, W. W. Dolan, W. P. Dyke, E. E. Martin, and J. K. Trolan, "Determination of the surface tension and surface migration constants for tungsten," *Phys. Rev.*, vol. 117, no. 6, p. 1452, 1960.

[49] L. C. Crouser and R. W. Strayer, "No Title," *J. Met.*, vol. 13, p. 74, 1961.

[50] A. . Price, H. . Holl, and A. . Greenough, "The surface energy and self diffusion coefficient of solid iron above 1350°C," *Acta Metall.*, vol. 12, no. 1, pp. 49–58, Jan. 1964.

[51] D. Hull, P. Beardmore, and A. Valintine, "Crack propagation in single crystals of tungsten," *Philos. Mag.*, vol. 12, no. 119, pp. 1021–1041, 1965.

[52] I. L. Sokolskaya, K. Noimann, and E. Kloze, *Sov. Phys. - Solid State*, vol. 6, p. 1126, 1964.

[53] E. D. Hondros, "The Influence of Phosphorus in Dilute Solid Solution on the Absolute Surface and Grain Boundary Energies of Iron," *Proc. R. Soc. London A Math. Phys. Eng. Sci.*, vol. 286, no. 1407, pp. 479–498, Aug. 1965.

[54] P. C. Bettler and C. G. Barnes, *Surf. Sci.*, vol. 10, p. 165, 1968.

[55] B. C. Allen, *Trans. Met. Soc. AIME*, vol. 236, p. 903, 1966.

[56] E. D. Hondros, "Interfacial Segregation of Nitrogen in Iron," *Met. Sci.*, vol. 1, no. 1, pp. 36–39, Jan. 1967.

[57] B. C. Allen, Final Report AD 637 793, Pt. 4, 1968.

[58] E. . Hondros, "The effect of adsorbed oxygen on the surface energy of B.C.C. iron," *Acta Metall.*, vol. 16, no. 11, pp. 1377–1380, Nov. 1968.

[59] E. N. Hodkin, M. G. Nicholas, and D. M. Poole, "The surface energies of solid molybdenum, niobium, tantalum and tungsten," *J. Less Common Met.*, vol. 20, no. 2, pp. 93–103, 1970.

[60] B. C. Allen, *Trans. Met. Soc. AIME*, vol. 245, p. 1621, 1969.

[61] T. A. Roth, "The surface and grain boundary energies of iron, cobalt and nickel," *Mater. Sci. Eng.*, vol. 18, no. 2, pp. 183–192, Apr. 1975.

[62] Z. I. Dranova, A. M. D'yachenko, and I. M. Mikhailovskiy, *Phys. Met. Met.*, vol. 31, p. 223, 1971.

[63] B. C. Allen, *J. Less-Common Met.*, vol. 29, p. 263, 1972.

[64] S. Tsurekawa, T. Tanaka, and H. Yoshinaga, "Grain boundary structure, energy and strength in molybdenum," *Mater. Sci. Eng.*, vol. A176, pp. 341–348, 1994.

[65] C. J. M. Jr. and V. Vitek, "The effects of segregated impurities on intergranular fracture energy," *Acta Metall.*, vol. 27, no. 4, pp. 507–513, 1979.

[66] M. L. Jokl, V. Vitek, and C. J. M. Jr, "A microscopic theory of brittle fracture in deformable solids: A relation between ideal work to fracture and plastic work," *Acta Metall.*, vol. 28, no. 11, pp. 1479–1488, 1980.

[67] J. B. Brosse, R. Fillit, and M. Biscondi, "Intrinsic intergranular brittleness of molybdenum," *Scr. Metall.*, vol. 15, no. 6, pp. 619–623, 1981.

[68] H. Kurishita, A. Ôishi, H. Kubo, and H. Yoshinaga, "Grain Boundary Fracture in Molybdenum Bicrystals with Various (110) Symmetric Tilt Boundaries," *J. Japan Inst. Met.*, vol. 26, no. 5, pp. 341–352, 1985.

[69] A. P. Sutton and R. W. Balluffi, *Interfaces in Crystalline Materials*. OUP Oxford, 1995.

[70] J. H. Bechtold and B. J. Shaw, "Fracture in the refractory metals," H. Liebowitz, Ed. Academic Press, 1969, pp. 371–398.

[71] J. Gilman, "Cleavage, ductility and tenacity in crystals," in *International Conference on Fracture*, 1959, pp. 193–224.

[72] R. J. Fields, T. Weerasooriya, and M. F. Ashby, "Fracture-mechanisms in pure iron, two austenitic steels, and one ferritic steel," *Metall. Trans. A*, vol. 11, no. 2, pp. 333–347, 1980.

[73] A. S. Drachinskiy, A. P. Kraynikov, A. P. Rudoy, V. N. Slyunyayev, and V. I. Trefilov, "Features of the variation in the cold shortness point of the interior and boundaries of grains of low-alloyed chromium and tungsten alloys," *Phys. Met. M*, vol. 57, no. 1, pp. 177–180, 1984.

[74] J. P. Perdew and A. Zunger, "Self-interaction correction to density-functional approximations for many-electron systems," *Phys. Rev. B*, vol. 23, p. 5048, 1981.

[75] J. P. Perdew, K. Burke, and M. Ernzerhof, "Generalized Gradient Approximation Made Simple," *Phys. Rev. Lett.*, vol. 77, p. 3865, 1996.

[76] J. P. Perdew, K. Burke, and M. Ernzerhof, "Erratum to: Generalized gradient approximation made simple," *Phys. Rev. Lett.*, vol. 78, p. 1396, 1997.

[77] R. Armiento and A. E. Mattsson, "Functional designed to include surface effects in self-consistent density functional theory," *Phys. Rev. B*, vol. 72, no. 8, p. 85108, 2005.

[78] A. E. Mattsson and R. Armiento, "Implementing and testing the AM05 spin density functional," *Phys. Rev. B*, vol. 79, no. 15, p. 155101, Apr. 2009.

[79] F. H. Featherston and J. R. Neighbours, "Elastic Constants of Tantalum, Tungsten, and Molybdenum," *Phys. Rev.*, vol. 130, no. 4, p. 1324, 1963.

[80] A. Magerl, B. Berre, and G. Alefeld, "Changes of the Elastic Constants of V, Nb, and Ta by Hydrogen and Deuterium," *Phys. Status Solidi A*, vol. 36, pp. 161–171, 1976.

[81] J. A. Rayne and B. S. Chandrasekhar, "Elastic Constants of Iron from 4.2 to 300 K," *Phys. Rev*, vol. 122, p. 1714, 1961.